Divalent ions tune the kinetics of a bacterial GTPase center rRNA folding transition from secondary to tertiary structure

ROBB WELTY,[1] SUZETTE A. PABIT,[2] ANDREA M. KATZ,[2] GEORGE D. CALVEY,[2] LOIS POLLACK,[2] and KATHLEEN B. HALL[1]

[1]Department of Biochemistry and Molecular Biophysics, Washington University School of Medicine, St. Louis, Missouri 63110, USA
[2]School of Applied and Engineering Physics, Cornell University, Ithaca, New York 14853, USA

ABSTRACT

Folding of an RNA from secondary to tertiary structure often depends on divalent ions for efficient electrostatic charge screening (nonspecific association) or binding (specific association). To measure how different divalent cations modify folding kinetics of the 60 nucleotide *E. coli* rRNA GTPase center, we combined stopped-flow fluorescence in the presence of Mg^{2+}, Ca^{2+}, or Sr^{2+} together with time-resolved small angle X-ray scattering (SAXS) in the presence of Mg^{2+} to observe the folding process. Immediately upon addition of each divalent ion, the RNA undergoes a transition from an extended state with secondary structure to a more compact structure. Subsequently, specific divalent ions modulate populations of intermediates in conformational ensembles along the folding pathway with transition times longer than 10 msec. Rate constants for the five folding transitions act on timescales from submillisecond to tens of seconds. The sensitivity of RNA tertiary structure to divalent cation identity affects all but the fastest events in RNA folding, and allowed us to identify those states that prefer Mg^{2+}. The GTPase center RNA appears to have optimized its folding trajectory to specifically utilize this most abundant intracellular divalent ion.

Keywords: RNA folding; SAXS; kinetics; rRNA GTPase center; stopped-flow fluorescence

INTRODUCTION

The 60 nucleotide (nt) GTPase center RNA (GAC) from 23S rRNA (Fig. 1) must adopt an intricate tertiary structure to be functional (Moazed et al. 1988; Xing and Draper 1996; Holmberg and Noller 1999; Cameron et al. 2002; Helgstrand et al. 2007; Harms et al. 2008; Gao et al. 2009; Voorhees et al. 2010; Sprink et al. 2016). In the ribosome, the GAC is bound by the prokaryotic L11 protein (L12 in eukaryotes); L11 binding requires that GAC adopt its tertiary fold (Blyn et al. 2000). The GAC is also the binding site for the peptide antibiotic thiostrepton (Blyn et al. 2000). GAC nucleotides make specific transient contacts with essential ribosome cofactors during translation (Harms et al. 2008), such that *E coli* lacking the GAC is not viable. In vivo, Mg^{2+} ions facilitate its transition from secondary structure to tertiary fold (Fig. 1). Previous in vitro experiments have measured its ion-dependent folding that identified a chelated Mg^{2+} ion (Grilley et al. 2007; Leipply and Draper 2011). GAC crystal structures, both free (courtesy of G. Conn) and bound to L11 (Wimberly et al. 1999; Conn et al. 2002), show two common sites of divalent ion association (Fig. 1) that are thought to be essential for proper tertiary structure formation. The critical importance of the GAC to translation motivates efforts to understand how it adopts its tertiary fold.

Tertiary structure in noncoding RNAs typically involves noncanonical interactions between nucleobases, riboses, and phosphates (Butcher and Pyle 2011). To date, such interactions are virtually impossible to predict de novo, yet they can be intricate (Tinoco and Bustamante 1999; Cruz and Westhof 2009) and intrinsic to function (Mortimer et al. 2014). As negatively charged polyelectrolytes, RNA recruits high concentrations of cations (Misra and Draper 1998; Shiman and Draper 2000; Draper 2008, 2013; Bowman et al. 2012) to screen its phosphates and this charge screening allows RNAs to explore compact conformations which facilitate tertiary interactions (Denesyuk and Thirumalai 2015). Some RNAs can chelate divalent ions to stabilize specific conformations (Conn et al. 2002; Leipply and Draper 2011). Mg^{2+} is the most common

Corresponding author: hallkathleen@wustl.edu
Article is online at http://www.rnajournal.org/cgi/doi/10.1261/rna.068361.118.

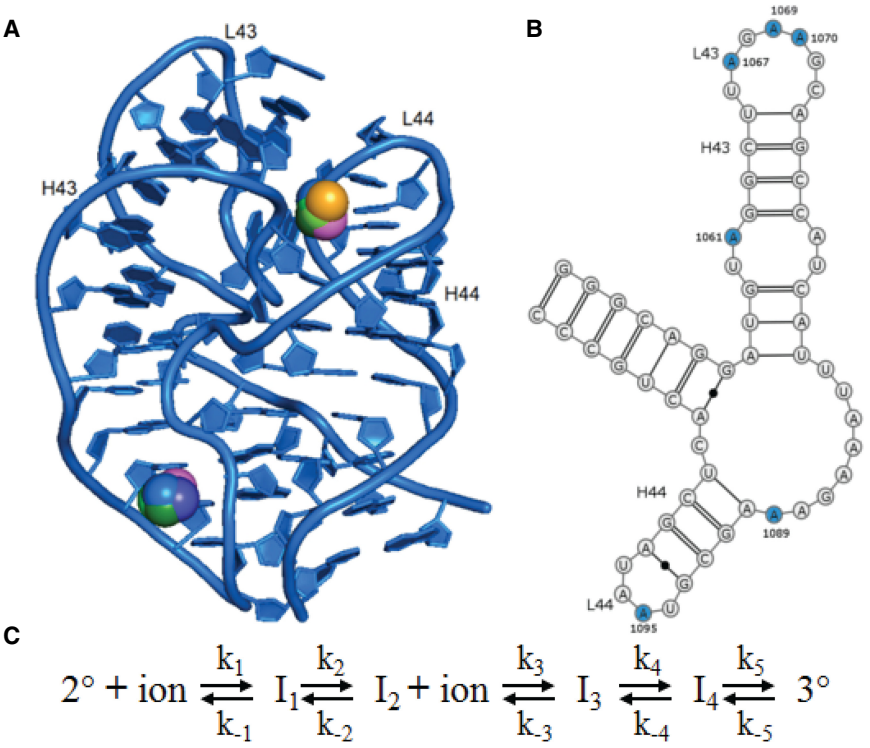

FIGURE 1. GAC structures and kinetic folding scheme. (*A*) Tertiary structure of *E. coli* GAC, with U1061A substitution (Conn et al. 2002). Divalent ion positions from a superposition of GAC crystal structures (pdb 1hc8, 1mms, 5d8h, 5dar, 4v8p, 4v4q); RNA is 1hc8. (*B*) Secondary structure from phylogenetic comparisons (Petrov et al. 2014). 2AP positions are labeled in blue. (*C*) Our model of the divalent ion-mediated (Me^{2+}) kinetic trajectory of tertiary folding (Welty and Hall 2016).

divalent cation used for RNA folding, as it can participate in different interactions through its six coordinated waters as well as direct coordination to phosphates.

Ion-induced RNA folding is mediated by multiple driving forces (Lipfert et al. 2010, 2014). Many RNA molecules undergo rapid compaction or "electrostatic collapse" after mixing with cations of different valences and atomic character (Russell et al. 2000, 2002; Das et al. 2003; Chauhan et al. 2005; Moghaddam et al. 2009; Roh et al. 2010). The earliest folding events can be attributed to electrostatic relaxation, where nonspecific charge screening by cations relaxes single-stranded loop and bulge regions, which allows for better conformational sampling (Bartley et al. 2003). When slower folding events are observed, they are typically attributed to specific ion binding (Gluick et al. 1997; Swisher et al. 2002) or the satisfaction of a conformational search (Pljevaljcić et al. 2005). An early example of time-resolved RNA folding used small angle X-ray scattering (SAXS) to probe the secondary-to-tertiary structure change in the Tetrahymena Group I intron (Russell et al. 2000). This 414 nt RNA has a modular secondary structure that was found to collapse upon addition of divalent ions, then rearrange itself into the correct tertiary fold. The Tetrahymena Group I intron has been a model system for many studies of RNA folding, even though it forms long-lived misfolded structures in vitro. Mutations that prevent or exacerbate misfolding have provided insights into how the RNA uses specific sites during folding, and how ions can modulate its tertiary interactions.

The GAC secondary structure is known from phylogenetic comparisons that also identified eighteen of its sixty nucleotides as invariant among all organisms (Gutell et al. 1992b). Its tertiary structure alone and in co-crystals with the L11 protein and in the context of the ribosome subunit (Gao et al. 2009) is preserved. In vitro solution chemical probing of secondary and tertiary structures of prokaryotic GAC RNAs are consistent with predictions and crystal structures (Leipply and Draper 2011). Biochemical experiments focusing on the *E. coli* GAC probed its sequence dependence (Ryan and Draper 1991; Lu and Draper 1994, 1995; Draper and Xing 1995), ion dependence (Wang et al. 1993; Bukhman and Draper 1997; Leipply and Draper 2010), and thermal stability (Shiman and Draper 2000; Draper et al. 2001; Leipply et al. 2009), creating a compendium of data on its physico-chemical properties. In *E. coli* GAC, a single substitution, U1061A, destabilizes the tertiary structure in monovalent ions, and effectively results in a requirement for divalent ions (Mg^{2+}) to adopt a stable tertiary structure (Lu and Draper 1994). Its Mg^{2+} requirement allows us to examine how this essential RNA element uses divalent ions to adopt its structure.

We are exploring the kinetic trajectory of the ion-induced conformational change from secondary structure to tertiary fold (Rau et al. 2015; Welty and Hall 2016). We replaced six adenosine nucleobases that crystal structures showed were not involved in hydrogen bonding (Wimberly et al. 1999; Conn et al. 2002) with the fluorescent base 2-aminopurine (Fig. 1). Stopped-flow fluorescence investigations of Mg^{2+}-induced folding revealed multiple states along the GAC folding trajectory (Fig. 1; Welty and Hall 2016).

Now, we have examined GAC folding kinetics in the presence of Ca^{2+} and Sr^{2+}. An earlier study of the GAC stability in the presence of Ca^{2+}, Sr^{2+}, and Mg^{2+} identified two binding sites with differential affinities for these ions (Bukhman and Draper 1997) that could affect the states along the kinetic trajectory we proposed (Welty and Hall 2016). Additionally, time-resolved and steady-state SAXS

experiments allow us to connect structural insights of conformational ensembles to the mechanistic folding model. Time-resolved SAXS data show a rapid compaction of the GAC within 10 msec after Mg^{2+} addition as seen in other small RNA molecules (Russell et al. 2002; Das et al. 2003; Perez-Salas et al. 2004; Takamoto et al. 2004; Plumridge et al. 2018). Our new results show that initial GAC contacts with divalent ions are electrostatic, but subsequent GAC/divalent ion interactions are ion-specific. The three divalent ions lead to biased subpopulations in the dynamic equilibria of GAC structures within states along folding routes, and reveal how Mg^{2+} ions have a unique role in folding of the GAC.

RESULTS

Divalent ion titrations

UV absorbance and steady state SAXS

For all our experiments, we use a variant of *E. coli* GAC containing the U1061A substitution. Position 1061 is not conserved in GAC sequences; most eukaryotic GAC's have G1061, and some archaea have A1061 (Gutell et al. 1992a). In the background of the *E. coli* sequence, A1061 destabilizes any tertiary structure that might form in the absence of divalent ions, but has increased stability in the presence of Mg^{2+} (Lu and Draper 1994). Sites of 2AP substitution were selected from phylogenetic comparisons and crystal structures: sites A1067, A1069, and A1061 are not conserved and do not contribute hydrogen bonds to the tertiary fold; A1070 and A1095 are invariant, but do not make tertiary contacts (A1095 contacts cofactors). We assessed secondary and tertiary structure stability for all 2AP constructs by thermal denaturation in UV absorbance measurements, as established by the Draper lab (Ryan and Draper 1991).

To evaluate the role of ions on folding, we compared the change in absorbance and the change in SAXS properties of the GAC during titrations with $MgCl_2$, $CaCl_2$, and $SrCl_2$. Ca^{2+}, Sr^{2+}, and Mg^{2+} are alkaline earth metal cations that differ in their hydrated radii (4.14, 4.14, 4.28 Å, respectively [Conway 1981]). All have closed-shell electron orbitals, and all are associated with at least six water molecules in solution. Previous studies (Bukhman and Draper 1997) of *E. coli* GAC U1061G stability in 1.6 M NH_4Cl upon addition of Ca^{2+}, Sr^{2+}, Ba^{2+}, or Mg^{2+}, identified two ion binding sites: One site bound tighter to ions with a smaller ionic radius ($Mg^{2+} > Ca^{2+} > Sr^{2+}$); the second site preference was ordered $Mg^{2+} > Ba^{2+} > Sr^{2+} > Ca^{2+}$. Now, we work in a background of 100 mM KCl (K^+ is more effective than Na^+ at stabilizing GAC structure [Lu and Draper 1994]) to measure the effects of Ca^{2+} and Sr^{2+} on the kinetics of GAC folding.

First in steady-state experiments, we find that all three divalent cations drive GAC tertiary structure formation, but they are not equivalent. The change in UV absorption upon titration with the ions reveals a progressive decrease in absorbance at 260 nm (Fig. 2A) as the GAC adopts its tertiary structure. We attribute the loss of absorbance to an increase in base stacking and corresponding hypochromicity (Grilley et al. 2007). Mg^{2+} drives the transition to the tertiary structure at lower concentrations than either Ca^{2+} or Sr^{2+}. Significantly, the final value of absorbance change is not identical, suggesting that the final folded states of the GAC differ with divalent ion.

Analogous steady-state SAXS measurements provide another measure of the folded tertiary state of the GAC. Titrations of the GAC with each divalent ion show a dramatic difference in the calculated radius of gyration (R_g)

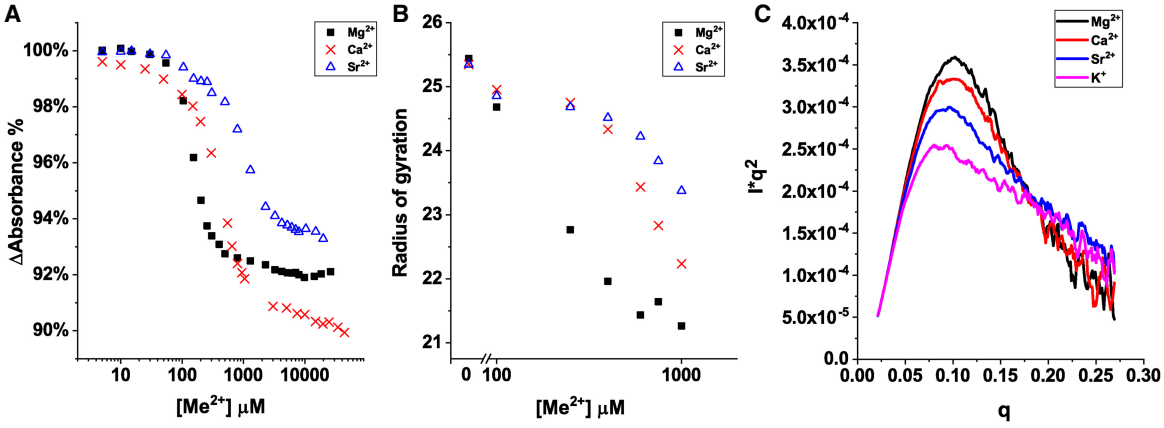

FIGURE 2. GAC tertiary structure ensemble is controlled by divalent ion identity. (*A*) Percent absorbance change at 260 nm of the GAC RNA upon titration with divalent ions. [GAC] = 2 μM; starting absorbance for each titration is the same within error. Data corrected for dilution with higher concentrations of ions. (*B*) Calculated *Rg* from steady-state SAXS measurements upon titration with divalent ions. (*C*) Kratky profiles from SAXS shows compaction from the extended states in KCl to more compact states in 1 mM divalent ions. [GAC] = 30 μM. All solutions contained 100 mM KCl, 10 mM sodium cacodylate (absorbance) or MOPSO (SAXS), pH 6.5 at 22°C.

of the RNA (Fig. 2B). SAXS profiles are shown as Kratky plots, $I \times q^2$ versus q (Fig. 2C), to illustrate the evolution of compaction from the extended state. GAC in K^+ shows a Kratky profile with a low peak and lightly sloping tail, characteristic of extended states. The Kratky profile of a more compact state shows a pronounced peak and a sharper decaying tail at high q. At 1 mM divalent ion concentration, GAC in $MgCl_2$ is more compact than in $CaCl_2$, which is more compact than in $SrCl_2$. For GAC in 1 mM $MgCl_2$, *Rg* averaged over 12 measurements taken at 6 beam runs was 21.3 ± 0.5 Å (20.2 Å–21.9 Å). (We note that our SAXS measurements and *Rg* values for GAC follow very stringent rules developed for analysis [Trewhella et al. 2017].) Please refer to the Supplemental Material for illustrative I versus q data and a Guinier fit for the GAC.) Unfortunately, SAXS experiments were limited to a final 1 mM concentration of ions due to interparticle interference effects at higher divalent ion concentrations. The R_g trend follows the change in absorbance, supporting the interpretation that the folded ensembles of the GAC are not identical for the three ions.

In contrast, calculating *Rg* from the co-crystal structure (PDB ID 1HC8, after stripping off the L11 CTD) gives a value of 17 Å using the program CRYSOL (Svergun et al. 1995). This difference implies that crystallization may inhibit some of the freedom of configurational motion in solution that allows the GAC to sample alternate conformations.

Previously, Grilley et al. (2007) also used SAXS to compare the envelopes of folded and unfolded GAC-U1061A. In a solution of 40 mM K^+ and 1 mM Mg^{2+} at 15°C, they calculated (with GNOM) *Rg* = 18 Å, and without Mg^{2+} *Rg* = 23–25 Å (40–150 mM K^+). The lower monovalent concentrations (40 mM KCl + Mg added) can lead to repulsive interactions at SAXS concentrations of nucleic acids, which could be misconstrued as lower *Rg* (Pabit et al. 2009, 2013), accounting for the disagreement between our values. In our experiments, we collected data at several GAC concentrations in several salt conditions (please see the Supplemental Material) to arrive at conditions where the data were consistent. We also used in-line and in-lab Size-Exclusion Chromatography (SEC) SAXS to probe for micro-aggregates that would inflate the *Rg* values. Although our value of *Rg* = 21.3 ± 0.5 Å for GAC in its tertiary fold is larger than the Grilley value, the trends from extended to compacted volume in the presence of Mg^{2+} are the same.

Fluorescence

For fluorescence experiments we utilized six individual constructs in which one Adenosine was replaced with 2-Aminopurine (2AP-GAC) (Dellinger et al. 2011). We have previously shown by thermal denaturation that these substitutions do not significantly alter GAC stability (Rau et al. 2015) (the GAC has a characteristic UV absorbance profile upon thermal denaturation). 2AP fluorescence reports local environmental changes (Jean and Hall 2001; Rachofsky et al. 2001; Rist and Marino 2001; Hall and Williams 2004; Sarkar et al. 2009), which in the GAC we have found are sensitive to the conformational change from secondary to tertiary structure (Welty and Hall 2016). Ion titrations of each 2AP-GAC showed that tertiary folding reaches equilibrium in Mg^{2+} and Ca^{2+} by 3 and 5 mM, respectively, whereas 100 mM Sr^{2+} is required. A comparison of the percent fluorescence change at each site in the presence of 5 mM and 100 mM Me^{2+} shows a consistent increase or decrease of fluorescence (Fig. 3). We interpret these data to indicate that local structural changes of the GAC are similar for the three divalent ions, and that its tertiary fold has formed.

Folding kinetics

Stopped-flow fluorescence

The time-trace of 2AP-GAC fluorescence for each 2AP site after addition of each divalent ion is shown in Figure 4. Concentrations of each added divalent ion were selected

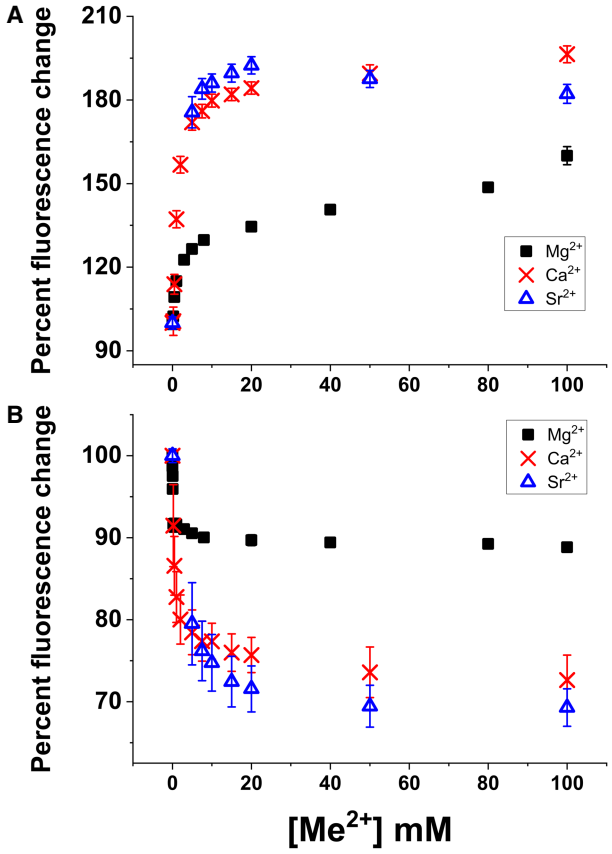

FIGURE 3. The RNA folds upon addition of divalent ions (Mg^{2+}, Ca^{2+}, Sr^{2+}). Titrations of 2AP-GAC fluorescence for (*A*) 2AP-1061 and (*B*) 2AP-1070 are shown. Other sites are analogous.

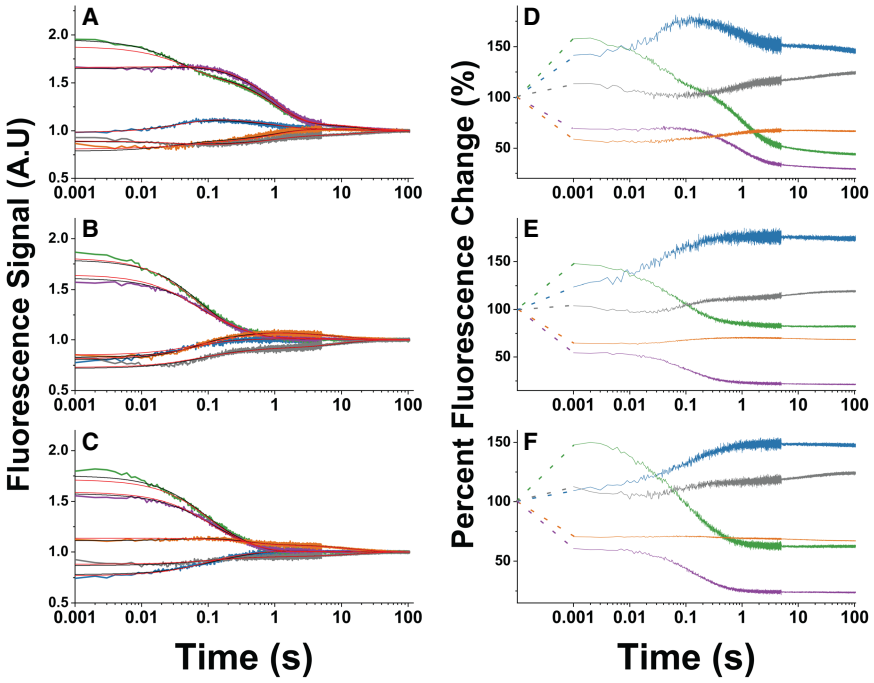

FIGURE 4. GAC tertiary folding kinetics. (*A–C*) Traces from stopped-flow fluorescence experiments show each 2AP-GAC RNA response to addition of each divalent ion at [Me^{2+}] = 20 mM (*top*: Mg^{2+}, *middle*: Ca^{2+}; *lower* Sr^{2}). 1061, blue; 1067, green; 1069, lavender; 1070, yellow; and 1095, gray. Each data trace is superimposed with its global fit from Equation 1. Traces have been offset to an ending value of 1 A.U. for comparison. (*D–F*) Traces replotted to show the rapid (~1 msec) 2AP fluorescence changes upon addition of divalent ions. Traces have been normalized to percent fluorescence change, with the starting value (without Me^{2+}) equal to 100%.

from titration experiments to ensure that saturation was reached (all stopped-flow fluorescence traces at all ion concentrations are shown in Supplemental Fig. 6A–C). Note that the shape of the fluorescent time-trace from several 2AP-GAC constructs varies with different divalent ions. Transitions in the presence of Mg^{2+} appear later in the timecourse, and the trace from 2AP-GAC 1061 is the most idiosyncratic. All traces collected with the same divalent ion at a given concentration were globally fit to the sum of three exponentials (Eq. 1),

$$y = y_0 + A_1 e^{-t/\tau_1} + A_2 e^{-t/\tau_2} + A_3 e^{-t/\tau_3} \quad (1)$$

which successfully reproduced the data, with the exception of AP1089, which has different transition times. The amplitudes differ with each 2AP site, but the rates are common to each. The resulting observed rates ($k_{obs} = 1/\tau$) partition into three timescales: 1–20 msec, 20–200 msec, and >200 msec (corresponding rates 1–50 sec^{-1}, 0.1 to 4 sec^{-1}, and 0.01 to 0.15 sec^{-1}), which are plotted for each ion in Figure 5.

This analysis reveals that GAC folding in Mg^{2+} is consistently different than in either Ca^{2+} or Sr^{2+}, revealing new insight into the mechanism of its ion-induced folding. The first transition with observed rate $k_{1,obs}$ is the most rapid. As we previously noted (Welty and Hall 2016), $k_{1,obs}$ for Mg^{2+} addition decreased with increased concentration of ion. This is a signature of a rate-limiting kinetic step that precedes a binding event (Galletto et al. 2005; Vogt and Di Cera 2012). For the GAC interaction with Mg^{2+}, that kinetic step corresponds to conformational changes of the RNA that occur before Mg^{2+} binds. In contrast, $k_{1,obs}$ in the presence of Ca^{2+} and Sr^{2+} increase with increasing ion concentrations, which is also consistent with an induced-fit mechanism (in the limit of rapid equilibrium); while perhaps not intuitively obvious, the analytical relationship has been demonstrated (Vogt and Di Cera 2012). In the induced-fit mechanism, Ca^{2+} and Sr^{2+} would associate with the GAC and "force it" to adopt a conformation. Both signatures are examples of conformational selection (Vogt and Di Cera 2013; Chakraborty and Di Cera 2017), but the mechanisms are distinct.

Observed rates of subsequent GAC folding transitions ($k_{2,obs}$ and $k_{3,obs}$) are consistently slower in the presence of Mg^{2+}, and are sensitive to the specific ion. We can interpret these data in terms of conformational ensembles: Mg^{2+} reduces rates of conformational sampling, while Ca^{2+}

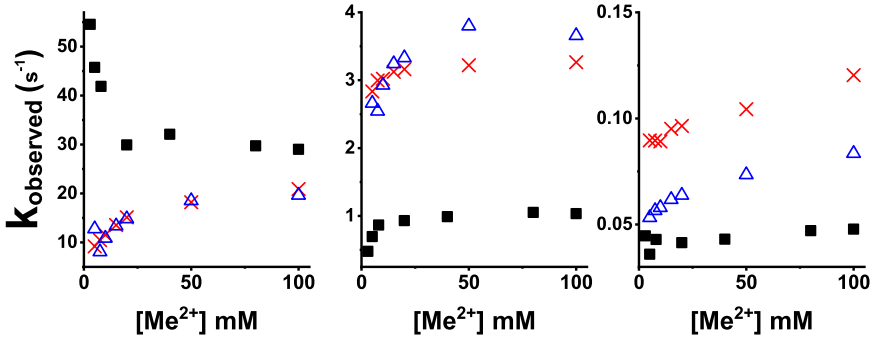

FIGURE 5. Global observed rates calculated from exponential fitting to Equation 1 as a function of divalent ion concentration ($1/\tau_n = k_{n,obs}$, $n = 1,2,3$). $k_{1,obs}$ (*left*) is the most rapid observed rate; $k_{2,obs}$ (*middle*) corresponds to the transition with the largest amplitude; $k_{3,obs}$ (*right*) is the slowest rate. Mg^{2+}, ■; Ca^{2+}, X; and Sr^{2+}, Δ.

and Sr^{2+} allow more rapid sampling possibly due to weaker association. As a consequence, different ions preferentially stabilize different conformations in the ensembles.

Time-resolved SAXS

In our time-resolved fluorescence experiments, GAC in 100 mM KCl without divalent ion is mixed with a solution of $MgCl_2$, $CaCl_2$ or $SrCl_2$ in 100 mM KCl at various concentrations. The dead time of the mixer is ~1 msec, so events that occur more rapidly cannot be directly observed. However, at the first detectable timepoint (~1 msec), we observe that all 2AP-GAC fluorescence intensities have changed from their starting values in KCl (when the GAC has only secondary structure). In Figure 4D–F, that starting fluorescence value is designated as 100%. Dotted lines indicate the jump of fluorescence intensity upon mixing with divalent ion solution. The trend at each site is independent of the specific divalent ion, although its amplitude is ion concentration-dependent.

We previously proposed that the rapid event in the fluorescence experiments was due to a rapid initial global compaction of the GAC upon Mg^{2+} addition (Welty and Hall 2016). Now, we use time-resolved SAXS to measure the scattering properties of the GAC during Mg^{2+}-induced folding. (Similar experiments in the TR-SAXS flowcell with $CaCl_2$ yielded unusable results caused by interparticle association, and the required Sr^{2+} concentration is too high for the apparatus.) Time points (0.01, 0.03, 0.05, 0.1, 0.3, and 1 sec) corresponded to analogous fluorescence measurements. *Rg* was calculated at each timepoint (Fig. 6A) from Guinier analysis; representative Kratky profiles are shown (Fig. 6B). TR-SAXS data show that the RNA forms a more compact state within 10 msec of the addition of divalent ions. Kratky profiles continue to evolve up to 1 sec approaching the final state ($t = \infty$) at *Rg* of ~22 Å, comparable to the steady-state value of 21.3 ± 0.5 Å in 1 mM $MgCl_2$. We conclude that indeed the fluorescence change that occurs in <1 msec in our stopped-flow fluorescence experiments is due to a global compaction of the GAC.

Numerical modeling of folding kinetics

The initial interaction of the GAC with divalent ions (<1 msec) is not described by Eq. 1. This in part led to our working model (Welty and Hall 2016) of the folding kinetics in the presence of Mg^{2+} that included six states (Fig. 1). In our model, the secondary structure (2°) transitions to intermediates I_1 and I_2 upon addition of divalent ion in <1 msec. Association of a single stoichiometric ion leads to I_3, which then samples conformations to result in a final ensemble that includes I_3, I_4, and the tertiary fold (3°). More complex kinetic mechanisms, both nonlinear and those with additional states, were unable to better fit the data.

Now, with three divalent ions, Mg^{2+}, Ca^{2+}, and Sr^{2+}, we describe all states along the folding trajectory analyzed by metaheuristic optimization algorithms (Hastie et al. 2009) to determine any similarities in their kinetic mechanisms (see Supplemental Material). While our kinetic scheme describes GAC folding in the presence of all three divalent ions, the analysis notably reveals that ion interactions with the RNA result in different rate constants and equilibrium populations (Table 1; Fig. 7).

The first GAC transition (<1 msec) is not divalent ion-specific (K_1; k_1, k_{-1} are identical), suggesting that the ions are there to neutralize phosphate charges and allow a close approach of chains. Significantly, rate constants k_{-4} and k_{-5} for Mg^{2+} are uniquely slow. These slow reverse rates effectively drive the GAC forward to its final conformation (3° in Fig. 1), as they limit its backward sampling of previous states. In contrast, the rate constants k_{-4} and k_{-5} in Ca^{2+} and Sr^{2+} are equal to or more rapid than their respective forward rates, and as a consequence, the final state of the GAC in these divalents will contain substantial populations of I_3, I_4, and 3° (Fig. 1). The critical ion property that alters these rate constants cannot be ascertained from our experiments. Ion charge density, hydrated radius, number of associated waters, polarizability, or ease of dehydration may all contribute. Curiously, the rate constants could reflect the difference in ion binding affinity

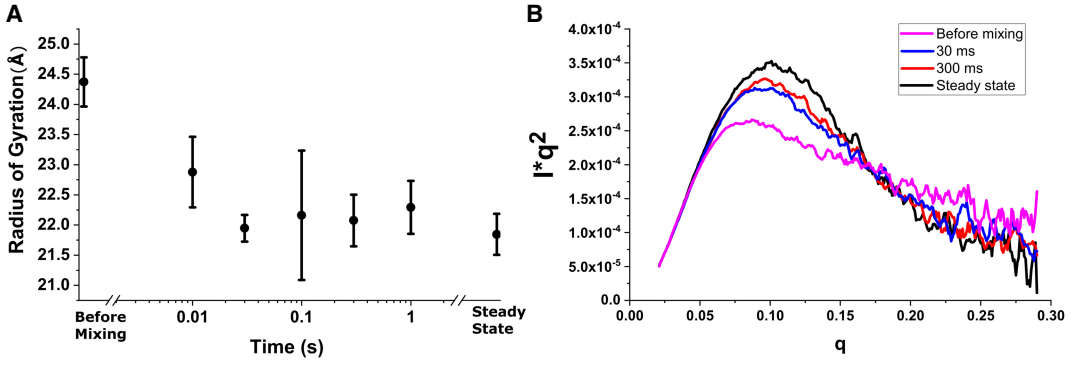

FIGURE 6. The GAC has a rapid response to addition of divalent ions. (*A*) TR-SAXS continuous mixer allows us to follow the change in *Rg* of the GAC as a function of time in the presence of Mg^{2+}. (*B*) Kratky plots for $t = 0$, $t = 30$ msec, $t = 300$ msec, $t =$ steady state along the trajectory.

TABLE 1. Rate constants along the GAC folding trajectory

	k_1 (sec-M)$^{-1}$	k_{-1} sec^{-1}	k_2 sec^{-1}	k_{-2} sec^{-1}	k_3 (sec-M)$^{-1}$	k_{-3} sec^{-1}	k_4 sec^{-1}	k_{-4} sec^{-1}	k_5 sec^{-1}	k_{-5} sec^{-1}
Mg^{2+}	130	2470	45	10	21	23.7	1.1	0.02	0.044	0.0017
Ca^{2+}	130	2470	36	12	26	28.1	1.8	2.0	0.028	0.097
Sr^{2+}	130	2470	23	9.6	42	20.2	0.84	2.0	0.0062	0.059

Rate constants (sec^{-1}) calculated from global fitting of rate equations. k_n is a forward rate constant; k_{-n} is the reverse rate constant.

of these three divalent ions (Bukhman and Draper 1997) [site one affinity: ($Mg^{2+} > Ca^{2+} > Sr^{2+}$); site two affinity: ($Mg^{2+} > Sr^{2+} > Ca^{2+}$)] noted in equilibrium binding experiments with the GAC.

Here we must introduce a caveat regarding the interpretation of intermediates in the kinetic model of GAC folding (Fig. 8). Classically, these intermediates have been associated with specific structures that undergo conformational changes along a path. As articulated by Dill and Chan, in their perspective on protein folding (Dill and Chan 1997), these intermediates are in fact ensembles of conformations. Distributions of conformations can be broad, and conformations are not restricted to a particular intermediate state. The concept of a rugged folding funnel seems made for descriptions of RNA folding: GAC folding has a "bumpy landscape" with its corresponding multiple state kinetics.

DISCUSSION

There is not a single tertiary structure of the GAC RNA. Instead, there is an ensemble that is best modeled as a dynamic equilibrium of folded states (I_3, I_4, and 3°). Indeed, previous work has shown that sequence variants of the GAC exhibit different stabilities under thermal denaturing conditions depending on the associated divalent ion (Bukhman and Draper 1997). This suggests two possible hypotheses: First, that the RNA has unique conformational states for each ion; Second, that the RNA accesses the same folded states but in different ion-specific proportions. Because our data sets from each ion can all be modeled by the same kinetic mechanism, we propose that there is ion-specific stabilization of different states within a common ensemble.

Other studies of RNA folding have arrived at similar conclusions. For example, observation of the flux of intermediates in the ion-dependent folding pathway of the Tetrahymena Group I intron RNA, and dynamic equilibria of RNAs observed using single molecule experiments (Heilman-Miller et al. 2001; McDowell et al. 2010; Wan et al. 2010; Suddala et al. 2015) are consistent with our second hypothesis. Specifically, Tetrahymena Group I intron was shown to undergo electrostatic collapse, also referred to as electrostatic relaxation or compaction, as the first response to divalent ions (Russell et al. 2000, 2002; Das et al. 2003). Previous studies have used equilibrium ion titrations to measure RNA tertiary folding, the more sophisticated of which typically invoke either cooperative folding mechanisms (Fang et al. 2002; Behrouzi et al. 2012; Strulson et al. 2014) or the partial ion interaction coefficient framework (Record et al. 1978). The assumptions and complications of these approaches have been discussed by Lipfert et al. (2010, 2014). If an RNA tertiary structure is composed of multiple states in a dynamic equilibrium with similar spectroscopic signals, then standard binding density functions will not accurately describe the ion associations. Our

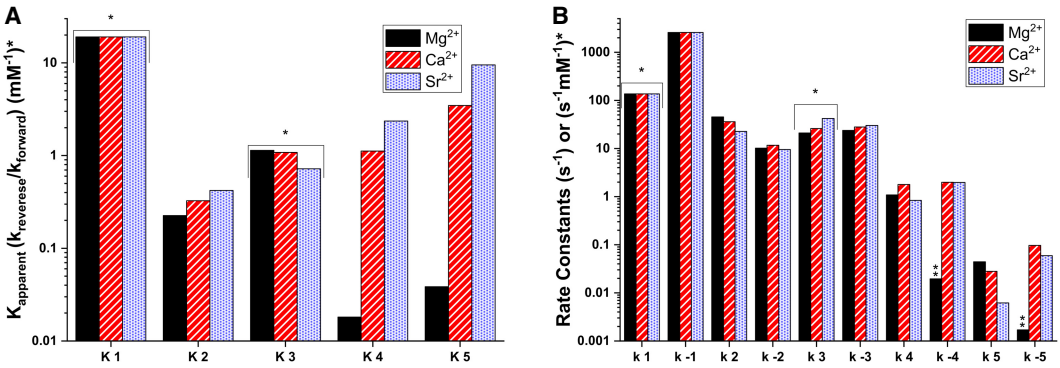

FIGURE 7. Apparent equilibrium constants (K_n) and calculated rate constants (k_n) for GAC tertiary folding. *K1 and *K3 reflect bimolecular interactions between RNA and ions ($s^{-1}mM^{-1}$). k_n is forward rate constant; k_{-n} is reverse rate constant. (**) *Upper* limit values. Slower rates do not change the quality of fit.

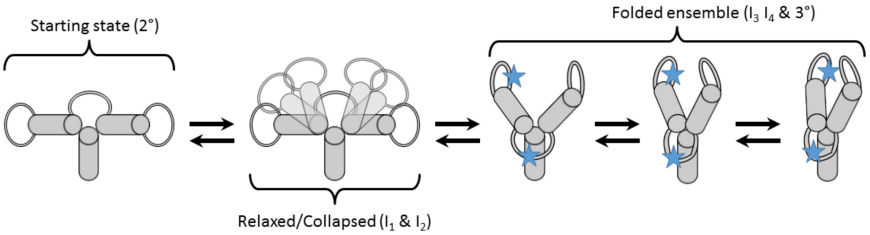

FIGURE 8. A conceptual model of GAC folding. From *left*: Starting from the secondary structure (State 1), an ensemble of conformations is present upon addition of divalent ions (States 2 and 3); a stoichiometric Me^{2+} ion can bind to some structures, leading to formation of tertiary interactions (including base triples) that staple the hairpins together; the three-way junction is collapsed to form a triloop (States 4,5,6). Blue stars correspond to two sites in crystal structures where divalent ions are located.

kinetics experiments reveal the presence of ion-dependent transitions that equilibrium experiments cannot see.

Dissecting RNA tertiary folding trajectories can prove challenging and has only been attempted for a few RNA molecules (Deras et al. 2000; Ralston et al. 2000; Keller et al. 2014). The difficulty arises in trying to define often short-lived intermediates that are very difficult to identify and quantify. Previous attempts have utilized a range of time-resolved techniques such as footprinting (Sclavi et al. 1998; Silverman et al. 2000; Shcherbakova et al. 2004), scattering (both X-ray and neutron) (Russell et al. 2000; Das et al. 2003; Perez-Salas et al. 2004; Moghaddam et al. 2009; Roh et al. 2010; Pollack 2011), as well as fluorescence (Chauhan et al. 2009; Haller et al. 2011; Buskiewicz and Burke 2012; St-Pierre et al. 2014; Frener and Micura 2016). Our experiments directly observe continuous changes in the orientations and stacking of the 2AP nucleobases (local events) as well as changes in the global conformational ensemble observed via SAXS during the transition from secondary structure to tertiary folds.

Separating the effects of nonspecific ion association and specific ion binding to nucleic acids is a complex and nontrivial problem. In the context of equilibrium RNA folding the energetic contributions of nonspecific association and binding are linked, and not independently measurable. Examining the kinetics of folding can help disentangle both effects by attempting to discover discrete binding events. Discrete binding events behave according to mass action laws, however nonspecific interactions, such as counterions with polyelectrolytes, do not (Wyman and Gill 1990). It is possible that there are nonspecific ion association effects that mimic stoichiometric binding to the GAC; however, this is unlikely due to the consistency of the model when accounting for three different cations at varying concentrations.

The identity of the ion alters both uni-molecular reactions (conformational changes) and bi-molecular reactions (discrete ion binding). The model in Figure 1 has two ion binding/unbinding steps; if the nature of nonspecific interactions were identical across all three cations, then only these rate constants would change. However, all rate constants, aside from k_1/k_{-1}, are modulated differently by each cation. These findings further support the hypothesis that the GAC "binds" each of these ions, although it does so with different affinities. Binding could be chelation, hydrogen bonding, and/or polarization; the differences could account for affinities and rate constants. Our data indicate that folding rates and equilibrium populations of RNA can be tuned by ion identity.

In cells, the GAC will be surrounded by K^+ and Mg^{2+} ions, both of which are preferred for its folding. Because it is a small autonomous structural element, it can adopt its secondary structure as it is being transcribed. After its final stem has formed, it can fold into its tertiary structure, and the folding trajectory that we describe here is a plausible model. In prokaryotes, the L11 protein could be present; L11 can bind to the GAC before it folds, and might be thought of as a (nonessential) chaperone.

MATERIALS AND METHODS

All GAC RNAs containing a single site 2-aminopurine were chemically synthesized by Agilent (Dellinger et al. 2011). GAC molecules were also transcribed using T7 RNA polymerase by run-off transcription (Milligan et al. 1987). All RNAs were purified by denaturing gel electrophoresis and dialyzed against 0.2 M EDTA, then against deionized distilled water. Solutions were lyophilized to concentrate the RNA, which was stored at −20°C until needed. To fold GAC into its secondary structure in buffer (no divalent ions), solutions were heated at 65° for 30 min and cooled to room temperature on the bench top (Leipply and Draper 2011). All experiments were performed in a buffer background of 10 mM sodium cacodylate and 100 mM KCl at pH 6.5. All stock solutions were passed through 0.45 µm cellulose nitrate filters and stored in the plastic reservoir (Nalgene).

Equilibrium fluorescence measurements were collected at 2 µM 2AP-RNA on a Photon Technology International spectrofluorometer at 20 ± 0.1°C. Samples were excited at 305 nm, and emission was measured at 368 nm wavelength. Absorption measurements were taken on a Cary 100Bio absorption spectrophotometer. Stopped-flow measurements were made on an Applied Photophysics SX-20 stopped-flow spectrometer 20 ± 0.1°C. RNA concentration for stopped-flow fluorescence was 100 nM (final), and for absorbance, 2 µM. Stopped-flow data were averaged and normalized with MATLAB (MathWorks), and globally fit using the originPRO (OriginLab Corp) software package. The basis for application of genetic algorithms to determine rate constants is detailed in the Supplemental Material.

All RNAs used in SAXS experiments were transcribed with T7 RNA polymerase (Milligan et al. 1987). Buffer conditions for SAXS experiments were 10 mM MOPSO, 100 mM KCl, pH 6.5.

Divalent ions were added to the RNA immediately prior to the SAXS measurements or mixed within the flow cell for the time-resolved SAXS (TR-SAXS) measurements. For static SAXS measurements, RNA concentrations were 30 and 60 µM and for TR-SAXS, 75–100 µM GAC.

All SAXS data were collected at the Cornell High Energy Synchrotron Source (CHESS). Steady state SAXS measurements were made using the BioSAXS setup at the G1 beamline (Supplemental Fig. S1) with x-ray energy of 9.924 keV and a beam size of 250 μm^2. Liquid samples were loaded in a 1.5 mm quartz capillary and the samples were oscillated to avoid radiation damage. Measurements were made using the Pilatus 100K detector over 20 sec with a 1 sec integration time. Time resolved SAXS (TR-SAXS) measurements were collected at the same G1 beamline with a home-built continuous flow mixer setup (Supplemental Fig. S4) using 11.18 keV x-rays that passed through a 50 µm scatterless pinhole. In the continuous-flow mixer setup, GAC in buffer and 100 mM KCl flows in the inner channel, and buffer with 20 mM $MgCl_2$ and 100 mM KCl flows in the outer channel. Mixing was facilitated by coaxial diffusion of Mg^{2+} ions into the sample as described previously (Pabit and Hagen 2002; Calvey et al. 2016; Plumridge et al. 2018). To collect TR-SAXS images, the flow cell was moved with respect to the x-ray beam to coincide with a particular mixing time point (Supplemental Table S1). Buffer background profiles were collected by turning off the sample flow. TR-SAXS experiments used an Eiger 1 M detector. All SAXS data were processed using BioXTAS RAW (Hopkins et al. 2017) and in-house MATLAB scripts. The reported radii of gyrations (*Rg*) were calculated from a Guinier Analysis (Supplemental Fig. S3), and the Kratky profiles, plots of $I \times q^2$ versus q, are shown to emphasize shape changes in the high-q region. More information on the SAXS experiments and the TR-SAXS flow cell are in the Supplemental Material.

SUPPLEMENTAL MATERIAL

Supplemental material is available for this article.

ACKNOWLEDGMENTS

We thank Michael Rau for many discussions and the figure showing conserved ion occupancy. We thank Professor Roberto Galletto for the use of his stopped-flow spectrometer. 2AP-GAC RNAs were received from Agilent Labs, and we especially thank Dr. Laura-Kay Bruhn and Dr. Doug Dellinger for making these experiments possible. We thank Professor Graeme Conn for sharing his GAC crystal structure. This work was supported by funds from Washington University and initially by the National Institutes of Health (grant R01-GM098102 to K.B.H.). Funding to L.P. is from the National Institutes of Health (R01-GM085062 and R35-GM122514) and the National Science Foundation through Science and Technology Center grant 1231306. The Cornell High Energy Synchrotron Source (CHESS) is supported by the National Science Foundation award DMR-1332208, using the Macromolecular Diffraction at CHESS (MacCHESS) facility, which is supported by award GM-103485 from the National Institutes of Health.

Received August 9, 2018; accepted September 20, 2018.

REFERENCES

Bartley LE, Zhuang X, Das R, Chu S, Herschlag D. 2003. Exploration of the transition state for tertiary structure formation between an RNA helix and a large structured RNA. *J Mol Biol* **328:** 1011–1026.

Behrouzi R, Roh JH, Kilburn D, Briber RM, Woodson SA. 2012. Cooperative tertiary interaction network guides RNA folding. *Cell* **149:** 348–357.

Blyn LB, Risen LM, Griffey RH, Draper DE. 2000. The RNA-binding domain of ribosomal protein L11 recognizes an rRNA tertiary structure stabilized by both thiostrepton and magnesium ion. *Nucleic Acids Res* **28:** 1778–1784.

Bowman JC, Lenz TK, Hud NV, Williams LD. 2012. Cations in charge: magnesium ions in RNA folding and catalysis. *Curr Opin Struct Biol* **22:** 262–272.

Bukhman YV, Draper DE. 1997. Affinities and selectivities of divalent cation binding sites within an RNA tertiary structure. *J Mol Biol* **273:** 1020–1031.

Buskiewicz IA, Burke JM. 2012. Folding of the hammerhead ribozyme: pyrrolo-cytosine fluorescence separates core folding from global folding and reveals a pH-dependent conformational change. *RNA* **18:** 434–448.

Butcher SE, Pyle AM. 2011. The molecular interactions that stabilize RNA tertiary structure: RNA motifs, patterns, and networks. *Acc Chem Res* **44:** 1302–1311.

Calvey GD, Katz AM, Schaffer CB, Pollack L. 2016. Mixing injector enables time-resolved crystallography with high hit rate at X-ray free electron lasers. *Struct Dyn* **3:** 054301.

Cameron DM, Thompson J, March PE, Dahlberg AE. 2002. Initiation factor IF2, thiostrepton and micrococcin prevent the binding of elongation factor G to the *Escherichia coli* ribosome. *J Mol Biol* **319:** 27–35.

Chakraborty P, Di Cera E. 2017. Induced fit is a special case of conformational selection. *Biochemistry* **56:** 2853–2859.

Chauhan S, Caliskan G, Briber RM, Perez-Salas U, Rangan P, Thirumalai D, Woodson SA. 2005. RNA tertiary interactions mediate native collapse of a bacterial group I ribozyme. *J Mol Biol* **353:** 1199–1209.

Chauhan S, Behrouzi R, Rangan P, Woodson SA. 2009. Structural rearrangements linked to global folding pathways of the Azoarcus group I ribozyme. *J Mol Biol* **386:** 1167–1178.

Conn GL, Gittis AG, Lattman EE, Misra VK, Draper DE. 2002. A compact RNA tertiary structure contains a buried backbone-K^+ complex. *J Mol Biol* **318:** 963–973.

Conway BE. 1981. *Ionic hydration in chemistry and biophysics.* Elsevier, Michigan.

Cruz JA, Westhof E. 2009. The dynamic landscapes of RNA architecture. *Cell* **136:** 604–609.

Das R, Kwok LW, Millett IS, Bai Y, Mills TT, Jacob J, Maskel GS, Seifert S, Mochrie SGJ, Thiyagarajan P, et al. 2003. The fastest global events in RNA folding: electrostatic relaxation and tertiary collapse of the *Tetrahymena* ribozyme. *J Mol Biol* **332:** 311–319.

Dellinger DJ, Timár Z, Myerson J, Sierzchala AB, Turner J, Ferreira F, Kupihár Z, Dellinger G, Hill KW, Powell JA, et al. 2011. Streamlined process for the chemical synthesis of RNA using 2′-*O*-thionocarbamate-protected nucleoside phosphoramidites in the solid phase. *J Am Chem Soc* **133:** 11540–11556.

Denesyuk NA, Thirumalai D. 2015. How do metal ions direct ribozyme folding? *Nat Chem* **7:** 793–801.

Deras ML, Brenowitz M, Ralston CY, Chance MR, Woodson SA. 2000. Folding mechanism of the *Tetrahymena* ribozyme P4-P6 domain. *Biochemistry* **39:** 10975–10985.

Dill KA, Chan HS. 1997. From Levinthal to pathways to funnels. *Nat Struct Biol* **4:** 10–19.

Draper DE. 2008. RNA folding: thermodynamic and molecular descriptions of the roles of ions. *Biophys J* **95:** 5489–5495.

Draper DE. 2013. Folding of RNA tertiary structure: linkages between backbone phosphates, ions, and water. *Biopolymers* **99:** 1105–1113.

Draper DE, Xing Y. 1995. Protein recognition of a ribosomal RNA tertiary structure. *Nucleic Acids Symp Ser* **33:** 5–7.

Draper DE, Bukhman YV, Gluick TC. 2001. Thermal methods for the analysis of RNA folding pathways. *Curr Protoc Nucleic Acid Chem* **Chapter 11:** Unit 11.3.

Fang XW, Thiyagarajan P, Sosnick TR, Pan T. 2002. The rate-limiting step in the folding of a large ribozyme without kinetic traps. *Proc Natl Acad Sci* **99:** 8518–8523.

Frener M, Micura R. 2016. Conformational rearrangements of individual nucleotides during RNA-ligand binding are rate-differentiated. *J Am Chem Soc* **138:** 3627–3630.

Galletto R, Jezewska MJ, Bujalowski W. 2005. Kinetics of allosteric conformational transition of a macromolecule prior to ligand binding: analysis of stopped-flow kinetic experiments. *Cell Biochem Biophys* **42:** 121–144.

Gao Y-G, Selmer M, Dunham CM, Weixlbaumer A, Kelley AC, Ramakrishnan V. 2009. The structure of the ribosome with elongation factor G trapped in the posttranslocational state. *Science* **326:** 694–699.

Gluick TC, Gerstner RB, Draper DE. 1997. Effects of Mg^{2+}, K^+, and H^+ on an equilibrium between alternative conformations of an RNA pseudoknot. *J Mol Biol* **270:** 451–463.

Grilley D, Misra V, Caliskan G, Draper DE. 2007. Importance of partially unfolded conformations for Mg^{2+}-induced folding of RNA tertiary structure: structural models and free energies of Mg^{2+} interactions. *Biochemistry* **46:** 10266–10278.

Gutell RR, Power A, Hertz GZ, Putz EJ, Stormo GD. 1992a. Identifying constraints on the higher-order structure of RNA: continued development and application of comparative sequence analysis methods. *Nucleic Acids Res* **20:** 5785–5795.

Gutell RR, Schnare MN, Gray MW. 1992b. A compilation of large subunit (23S- and 23S-like) ribosomal RNA structures. *Nucleic Acids Res* **20:** 2095–2109.

Hall KB, Williams DJ. 2004. Dynamics of the IRE RNA hairpin loop probed by 2-aminopurine fluorescence and stochastic dynamics simulations. *RNA* **10:** 34–47.

Haller A, Soulière MF, Micura R. 2011. The dynamic nature of RNA as key to understanding riboswitch mechanisms. *Acc Chem Res* **44:** 1339–1348.

Harms JM, Wilson DN, Schluenzen F, Connell SR, Stachelhaus T, Zaborowska Z, Spahn CMT, Fucini P. 2008. Translational regulation via L11: molecular switches on the ribosome turned on and off by thiostrepton and micrococcin. *Mol Cell* **30:** 26–38.

Hastie T, Tibshirani R, Friedman J. 2009. *The elements of statistical learning*. Springer, New York.

Heilman-Miller SL, Pan J, Thirumalai D, Woodson SA. 2001. Role of counterion condensation in folding of the *Tetrahymena* ribozyme. II. Counterion-dependence of folding kinetics. *J Mol Biol* **309:** 57–68.

Helgstrand M, Mandava CS, Mulder FAA, Liljas A, Sanyal S, Akke M. 2007. The ribosomal stalk binds to translation factors IF2, EF-Tu, EF-G and RF3 via a conserved region of the L12 C-terminal domain. *J Mol Biol* **365:** 468–479.

Holmberg L, Noller HF. 1999. Mapping the ribosomal RNA neighborhood of protein L11 by directed hydroxyl radical probing. *J Mol Biol* **289:** 223–233.

Hopkins JB, Gillilan RE, Skou S. 2017. BioXTAS RAW: improvements to a free open-source program for small-angle X-ray scattering data reduction and analysis. *J Appl Crystallogr* **50:** 1545–1553.

Jean JM, Hall KB. 2001. 2-Aminopurine fluorescence quenching and lifetimes: role of base stacking. *Proc Natl Acad Sci* **98:** 37–41.

Keller BG, Kobitski A, Jäschke A, Nienhaus GU, Noé F. 2014. Complex RNA folding kinetics revealed by single-molecule FRET and hidden Markov models. *J Am Chem Soc* **136:** 4534–4543.

Leipply D, Draper DE. 2010. Dependence of RNA tertiary structural stability on Mg^{2+} concentration: interpretation of the Hill equation and coefficient. *Biochemistry* **49:** 1843–1853.

Leipply D, Draper DE. 2011. Evidence for a thermodynamically distinct $Mg2^+$ ion associated with formation of an RNA tertiary structure. *J Am Chem Soc* **133:** 13397–13405.

Leipply D, Lambert D, Draper DE. 2009. Ion-RNA interactions thermodynamic analysis of the effects of mono- and divalent ions on RNA conformational equilibria. *Methods Enzymol* **469:** 433–463.

Lipfert J, Sim AYLL, Herschlag D, Doniach S. 2010. Dissecting electrostatic screening, specific ion binding, and ligand binding in an energetic model for glycine riboswitch folding. *RNA* **16:** 708–719.

Lipfert J, Doniach S, Das R, Herschlag D. 2014. Understanding nucleic acid–ion interactions. *Annu Rev Biochem* **83:** 813–841.

Lu M, Draper DE. 1994. Bases defining an ammonium and magnesium ion-dependent tertiary structure within the large subunit ribosomal RNA. *J Mol Biol* **244:** 572–585.

Lu M, Draper DE. 1995. On the role of rRNA tertiary structure in recognition of ribosomal protein L11 and thiostrepton. *Nucleic Acids Res* **23:** 3426–3433.

McDowell SE, Jun JM, Walter NG. 2010. Long-range tertiary interactions in single hammerhead ribozymes bias motional sampling toward catalytically active conformations. *RNA* **16:** 2414–2426.

Milligan JF, Groebe DR, Witherell GW, Uhlenbeck OC. 1987. Oligoribonucleotide synthesis using T7 RNA polymerase and synthetic DNA templates. *Nucleic Acids Res* **15:** 8783–8798.

Misra VK, Draper DE. 1998. On the role of magnesium ions in RNA stability. *Biopolymers* **48:** 113–135.

Moazed D, Robertson JM, Noller HF. 1988. Interaction of elongation factors EF-G and EF-Tu with a conserved loop in 23S RNA. *Nature* **334:** 362–364.

Moghaddam S, Caliskan G, Chauhan S, Hyeon C, Briber RMM, Thirumalai D, Woodson SA. 2009. Metal ion dependence of cooperative collapse transitions in RNA. *J Mol Biol* **393:** 753–764.

Mortimer SA, Kidwell MA, Doudna JA. 2014. Insights into RNA structure and function from genome-wide studies. *Nat Rev Genet* **15:** 469–479.

Pabit SA, Hagen SJ. 2002. Laminar-flow fluid mixer for fast fluorescence kinetics studies. *Biophys J* **83:** 2872–2878.

Pabit SA, Qiu X, Lamb JS, Li L, Meisburger SP, Pollack L. 2009. Both helix topology and counterion distribution contribute to the more effective charge screening in dsRNA compared with dsDNA. *Nucleic Acids Res* **37:** 3887–3896.

Pabit SA, Sutton JL, Chen H, Pollack L. 2013. Role of ion valence in the submillisecond collapse and folding of a small RNA domain. *Biochemistry* **52:** 1539–1546.

Perez-Salas UA, Rangan P, Krueger S, Briber RM, Thirumalai D, Woodson SA. 2004. Compaction of a bacterial group I ribozyme coincides with the assembly of core helices. *Biochemistry* **43:** 1746–1753.

Petrov AS, Bernier CR, Gulen B, Waterbury CC, Hershkovits E, Hsiao C, Harvey SC, Hud NV, Fox GE, Wartell RM, et al. 2014. Secondary structures of rRNAs from all three domains of life. *PLoS One* **9:** e88222.

Pljevaljčić G, Klostermeier D, Millar DP. 2005. The tertiary structure of the hairpin ribozyme is formed through a slow conformational search. *Biochemistry* **44:** 4870–4876.

Plumridge A, Katz AM, Calvey GD, Elber R, Kirmizialtin S, Pollack L. 2018. Revealing the distinct folding phases of an RNA three-helix junction. *Nucleic Acids Res* **46:** 7354–7365.

Pollack L. 2011. Time resolved SAXS and RNA folding. *Biopolymers* **95:** 543–549.

Rachofsky EL, Seibert E, Stivers JT, Osman R, Ross JB. 2001. Conformation and dynamics of abasic sites in DNA investigated by time-resolved fluorescence of 2-aminopurine. *Biochemistry* **40:** 957–967.

Ralston CY, Sclavi B, Brenowitz M, Sullivan M, Chance MR. 2000. The early folding intermediates of the *Tetrahymena* ribozyme are kinetically trapped. *J Biomol Struct Dyn* **17:** 195–200.

Rau MJ, Welty R, Tom Stump W, Hall KB. 2015. Formation of tertiary interactions during rRNA GTPase center folding. *J Mol Biol* **427:** 2799–2815.

Record MT, Anderson CF, Lohman TM. 1978. Thermodynamic analysis of ion effects on the binding and conformational equilibria of proteins and nucleic acids: the roles of ion association or release, screening, and ion effects on water activity. *Q Rev Biophys* **11:** 103–178.

Rist M, Marino J. 2001. Association of an RNA kissing complex analyzed using 2-aminopurine fluorescence. *Nucleic Acids Res* **29:** 2401–2408.

Roh JH, Guo L, Kilburn JD, Briber RM, Irving T, Woodson SA. 2010. Multistage collapse of a bacterial ribozyme observed by time-resolved small-angle X-ray scattering. *J Am Chem Soc* **132:** 10148–10154.

Russell R, Millett IS, Doniach S, Herschlag D. 2000. Small angle X-ray scattering reveals a compact intermediate in RNA folding. *Nat Struct Biol* **7:** 367–370.

Russell R, Millett IS, Tate MW, Kwok LW, Nakatani B, Gruner SM, Mochrie SGJ, Pande V, Doniach S, Herschlag D, et al. 2002. Rapid compaction during RNA folding. *Proc Natl Acad Sci* **99:** 4266–4271.

Ryan PC, Draper DE. 1991. Detection of a key tertiary interaction in the highly conserved GTPase center of large subunit ribosomal RNA. *Proc Natl Acad Sci* **88:** 6308–6312.

Sarkar K, Meister K, Sethi A, Gruebele M. 2009. Fast folding of an RNA tetraloop on a rugged energy landscape detected by a stacking-sensitive probe. *Biophys J* **97:** 1418–1427.

Sclavi B, Sullivan M, Chance MR, Brenowitz M, Woodson SA. 1998. RNA folding at millisecond intervals by synchrotron hydroxyl radical footprinting. *Science* **279:** 1940–1943.

Shcherbakova I, Gupta S, Chance MR, Brenowitz M. 2004. Monovalent ion-mediated folding of the Tetrahymena thermophila ribozyme. *J Mol Biol* **342:** 1431–1442.

Shiman R, Draper DE. 2000. Stabilization of RNA tertiary structure by monovalent cations. *J Mol Biol* **302:** 79–91.

Silverman SK, Deras ML, Woodson SA, Scaringe SA, Cech TR. 2000. Multiple folding pathways for the P4-P6 RNA domain. *Biochemistry* **39:** 12465–12475.

Sprink T, Ramrath DJF, Yamamoto H, Yamamoto K, Loerke J, Ismer J, Hildebrand PW, Scheerer P, Bürger J, Mielke T, et al. 2016. Structures of ribosome-bound initiation factor 2 reveal the mechanism of subunit association. *Sci Adv* **2:** e1501502.

St-Pierre P, McCluskey K, Shaw E, Penedo JC, Lafontaine DA. 2014. Fluorescence tools to investigate riboswitch structural dynamics. *Biochim Biophys Acta* **1839:** 1005–1019.

Strulson CA, Boyer JA, Whitman EE, Bevilacqua PC. 2014. Molecular crowders and cosolutes promote folding cooperativity of RNA under physiological ionic conditions. *RNA* **20:** 331–347.

Suddala KC, Wang J, Hou Q, Walter NG. 2015. Mg^{2+} shifts ligand-mediated folding of a riboswitch from induced-fit to conformational selection. *J Am Chem Soc* **137:** 14075–14083.

Svergun D, Barberato C, Koch MHJ. 1995. *CRYSOL*—a program to evaluate X-ray solution scattering of biological macromolecules from atomic coordinates. *J Appl Crystallogr* **28:** 768–773.

Swisher JF, Su LJ, Brenowitz M, Anderson VE, Pyle AM. 2002. Productive folding to the native state by a group II intron ribozyme. *J Mol Biol* **315:** 297–310.

Takamoto K, Das R, He Q, Doniach S, Brenowitz M, Herschlag D, Chance MR. 2004. Principles of RNA compaction: insights from the equilibrium folding pathway of the P4-P6 RNA domain in monovalent cations. *J Mol Biol* **343:** 1195–1206.

Tinoco I, Bustamante C. 1999. How RNA folds. *J Mol Biol* **293:** 271–281.

Trewhella J, Duff AP, Durand D, Gabel F, Guss JM, Hendrickson WA, Hura GL, Jacques DA, Kirby NM, Kwan AH, et al. 2017. 2017 publication guidelines for structural modelling of small-angle scattering data from biomolecules in solution: an update. *Acta Crystallogr D Struct Biol* **73:** 710–728.

Vogt AD, Di Cera E. 2012. Conformational selection or induced fit? A critical appraisal of the kinetic mechanism. *Biochemistry* **51:** 5894–5902.

Vogt AD, Di Cera E. 2013. Conformational selection is a dominant mechanism of ligand binding. *Biochemistry* **52:** 5723–5729.

Voorhees RM, Schmeing TM, Kelley AC, Ramakrishnan V. 2010. The mechanism for activation of GTP hydrolysis on the ribosome. *Science* **330:** 835–838.

Wan Y, Suh H, Russell R, Herschlag D. 2010. Multiple unfolding events during native folding of the *Tetrahymena* group I ribozyme. *J Mol Biol* **400:** 1067–1077.

Wang YX, Lu M, Draper DE. 1993. Specific ammonium ion requirement for functional ribosomal RNA tertiary structure. *Biochemistry* **32:** 12279–12282.

Welty R, Hall KB. 2016. Nucleobases undergo dynamic rearrangements during RNA tertiary folding. *J Mol Biol* **428:** 4490–4502.

Wimberly BT, Guymon R, McCutcheon JP, White SW, Ramakrishnan V. 1999. A detailed view of a ribosomal active site: the structure of the L11-RNA complex. *Cell* **97:** 491–502.

Wyman J, Gill SJ. 1990. *Binding and linkage: functional chemistry of biological macromolecules.* University Science Books, Mill Valley, CA.

Xing Y, Draper DE. 1996. Cooperative interactions of RNA and thiostrepton antibiotic with two domains of ribosomal protein L11. *Biochemistry* **35:** 1581–1588.